Drastic Improvement of Change Detection Results with Multilook Complex SAR Images Approach

Azzedine Bouaraba[1, *], Aichouche Belhadj-Aissa[2], and Damien Closson[3]

Abstract—Coherent Change Detection (CCD) is a powerful technique that uses Synthetic Aperture Radar (SAR) coherence to measure subtle ground changes in the imaged area. Unfortunately, the coherence estimator is biased for low coherence values, resulting in a highly degraded change detection performance. The spatial multilooking technique is typically used to improve coherence estimation but at the expense of spatial resolution. Actually, there are some SAR satellites that are able to deliver Multiple Look Complex (MLC) SAR images, which provide noticeable coherence bias reduction. In the present work, we investigate detection performance improvement that can be obtained through the use of MLC SAR images. The detection probability and false alarm are evaluated using experimental very high-resolution SAR data. After SAR image focusing and coherence estimation, the results indicate that the use of MLC SAR images with four looks allows for nearly 60% higher detection probability in the case of a low false alarm rate.

1. INTRODUCTION

Radar sensor is widely used in remote sensing as it offers the capability of acquiring images night and day, regardless of the weather conditions [1]. These advantages are critical in many practical situations because they extend the temporal and spatial applicability of radar-based techniques. As shown in Fig. 1, the radar moves in the azimuthal direction and looks in the range direction. The collected data are arranged in a two dimensional array to form the raw image. In a SAR signal processor, there are specific operations required to convert a raw data set into an interpretable image. Indeed, the raw radar data are not forming a useful image since point targets are spread out in azimuthal direction [2], a fact which is caused by the real aperture radar antenna. After the focusing process, the SAR image can be used in various applications such as Digital Elevation Model (DEM) generation [3], ground deformation monitoring, and detection of natural and man-made fine scale changes [4].

In CCD applications, the coherence is estimated through an interferometric (InSAR) processing of repeat-pass SAR image pair, for mapping subtle ground changes. As SAR image pixels are complex-valued numbers, subtle ground changes are not detected using SAR magnitude based methods since man-made activity randomizes only the InSAR phase. For example, foot and vehicle traffic that randomize the InSAR phase where they travel can be detected as a local loss of coherence but cannot be detected in the two SAR magnitude images [5]. Coherence is also used in some specific applications such as ground moving target indication [6] and damage-mapping after natural disaster [7].

In [8], the accuracy of the SAR coherence estimation was investigated, and it has been demonstrated that the sample coherence magnitude estimator is particularly biased for low coherence values. In addition to the presence of speckle in SAR data [9], the coherence bias causes the appearance of highly coherent pixels inside the changed area, thus considerably degrading the detection performance. Various

methods have been developed recently to better discern both the changed and the unchanged pixels. This was done by using a small window-size to preserve as much as possible subtle changes in the coherence image [10–12]. The development of coherence-based CCD techniques is still growing through deriving new metric [13] and new method [14] that improve the change detection performance.

The spatial multilooking technique, which consists in averaging neighboring SAR image pixels, is widely used to improve the SAR coherence estimation but at the expense of spatial resolution [8]. There is also another form namely temporal multilooking. Indeed, during scene imaging, a radar system continuously emits pulses with high repetition frequency. This means that the same ground target may reflect a large number of echoes toward the radar. As a result, one can use temporal multilooking by averaging multiple radar echoes during the image acquisition time. In this case, the image pixel resolution is preserved and the SAR data is designed as MLC, in contrast to the Single Look Complex (SLC) which is the standard SAR data type. Actually, there are only some SAR systems such as CosmoSky Med that permit delivering MLC images, and there is no recent study that shows the use of this type of data in change detection applications.

In the present work, we investigate detection performance improvement that may be obtained throughout the use of SAR MLC images. The very high resolution test data were obtained by an indoor experimental radar system. After the SAR image formation, using various focusing algorithms, the problem of coherence misestimation is introduced. The probability of detection and false alarm are evaluated to quantify the change detection performance improvement.

The present paper is organized as follows. In Section 2, we deal with SAR image formation whereas in Section 3, we address the problem of coherence misestimation and methods of bias reduction. In Section 4, we provide the characteristics of the radar system used in the experiments. In Section 5, we assess the performance of the obtained CCD results in terms of detection probability and false alarm by using experimental MLC SAR data. The conclusion is given in Section 6.

2. SAR IMAGE FORMATION

The geometry of the radar imaging system is shown in Fig. 1. The radar antenna (size $L \times D$) moves in the azimuthal direction and looks into the range direction. The swath width, or size of the illuminated area in the range direction, is determined by the elevation beamwidth which is equal to λ/D. This, together with the look angle, determines the imaged area. As the radar moves along, it flies in a straight line emitting short pulses at a rate called the Pulse Repetition Frequency (PRF). The returns of each one of these pulses make up a range line in the radar image. The pulse returns are arranged in parallel so as to form a raw image. Each pixel of the image has two associated coordinates: an **azimuth** time coordinate which gives the time the range line was imaged and a **range** time coordinate which gives the elapsed time between transmitting and receiving the pulse echo.

For a given distance antenna-target R, the azimuth resolution of the radar is given by $R\lambda/L$. It means that this resolution deteriorates as the distance R increases [2]. As a result, when a point target is illuminated by the radar antenna, it reflects backscattered energy that spreads mainly in azimuthal direction. The goal of SAR processing is to compress the raw data into a single point to reconstruct a useful SAR image.

As the radar data are complexly valued, the SAR processing algorithms can be divided into two classes, frequency domain algorithms and time domain algorithms.

Frequency domain algorithms are also called Fast Fourier Transform (FFT) based algorithms. On the other hand, time domain algorithms are called back-projection algorithms as well. The family of frequency domain algorithms are the primary methods for SAR image processing. The main algorithms are the Range Doppler Algorithm (RDA), the Chirp Scalling Algorithm (CSA) and the Omega-K Algorithm (ω-KA) [15], all of which are analyzed in the present work.

As the radar system continuously emits pulses with high PRF, a same ground target may reflect a large number of echoes toward radar [16]. As indicated in Fig. 2, at each azimuthal position, M range vectors are stored instead of 1 vector in the SLC data. This process will produce a radar cube of dimensions N_{az} (number of azimuth positions) by N_{rg} (number of range bins in fast time) by M (number of pulses in slow time) [16].

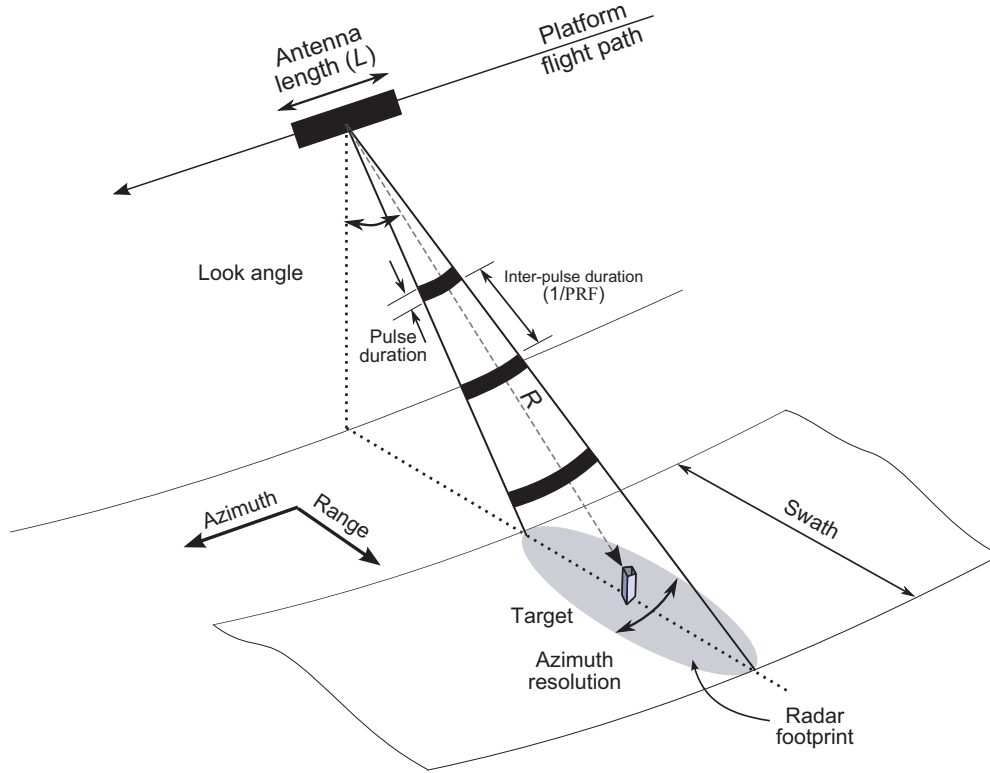The temporal multilooking occurs over M consecutive pulses (known as a coherent processing

Figure 1. Radar imaging system geometry.

interval) and consists in averaging multiple received radar echoes over the slow time. According to Fig. 2, the spatial resolution of the MLC SAR image is preserved as in the raw data. Unfortunately, MLC SAR images require additional processing resources and there are actually only a few operational SAR systems that are capable of delivering this type of data. In the following sections, we investigate coherence estimation and change detection improvement that may be obtained using the MLC SAR images.

3. COHERENCE ESTIMATION

SAR data are often modeled as a collection of spatially uncorrelated pixels drawn from a zero-mean circularly complex Gaussian distribution. Given $\underline{s}_1$ and $\underline{s}_2$ the two coregistred SAR images acquired over the same area at different times, the coherence is defined as the magnitude of the estimated complex cross-correlation coefficient, given by the formula [5]:

$$\widehat{\gamma} = |\widehat{\gamma}| \exp(j\phi) = \frac{\sum_{n=1}^{N} \underline{s}_{1,n} \underline{s}_{2,n}^*}{\sqrt{\sum_{n=1}^{N} |\underline{s}_{1,n}|^2 \sum_{n=1}^{N} |\underline{s}_{2,n}|^2}} \tag{1}$$

where $|\widehat{\gamma}|$ is the sample coherence that encodes the degree of scene similarity as a value in the range $[0, 1]$, N the number of samples, and ϕ the filtered InSAR phase.

As the InSAR phase is sensitive to changes in the spatial distribution of scatterers within a resolution cell, the CCD technique, which detects the low-coherence areas as changes, has the potential to detect subtle ground changes that may remain undetected using only SAR intensity images [12].

3.1. Estimation Bias

An analytical expression for the Probability density function (Pdf) of the SAR coherence estimator in Equation (1) was derived in [8] as a function of the real value of the coherence to be estimated $|\gamma|$
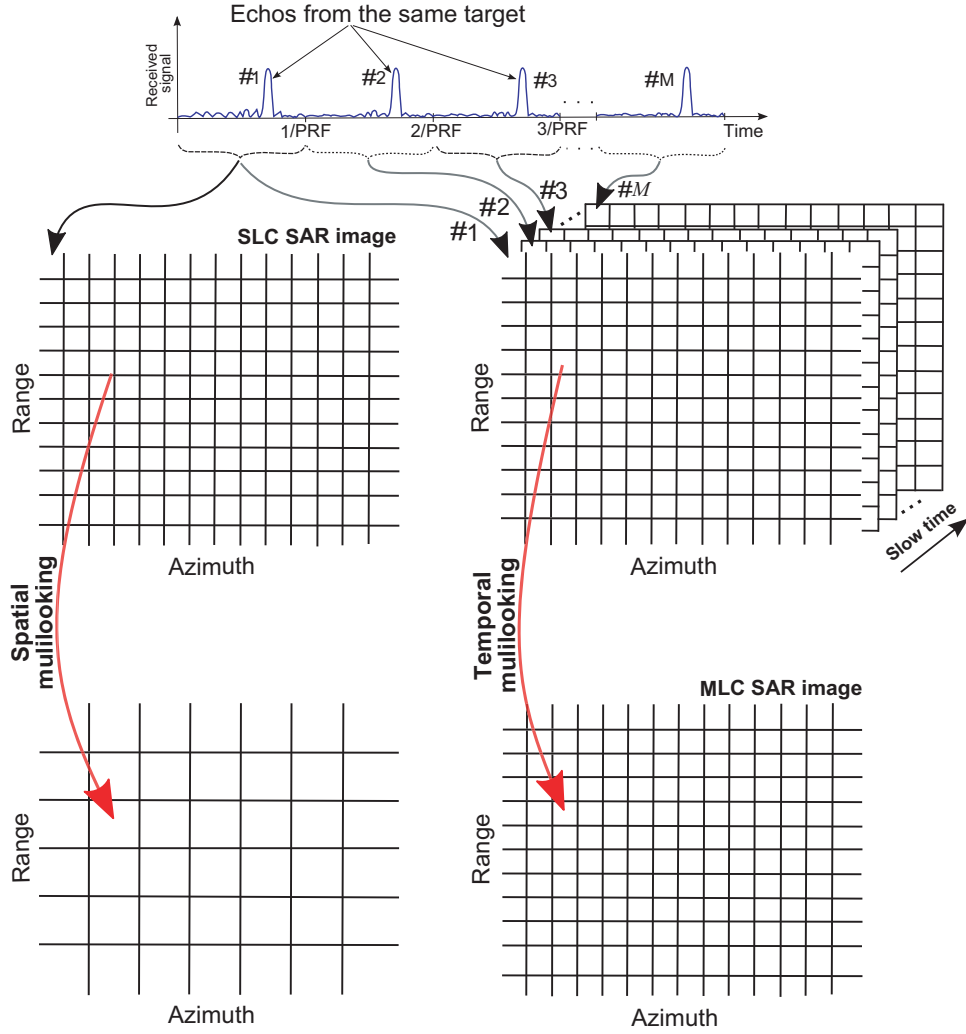
**Figure 2.** Spatial and temporal multilooking of the SAR images.

and the number of independent samples N. Here Γ denotes the gamma function and F the Gauss hypergeometric function.

$$\text{Pdf}(|\hat{\gamma}|) = 2(N-1)(1-|\gamma|^2)^N|\hat{\gamma}|(1-|\hat{\gamma}|^2)^{N-2} \times_2 F_1(N, N; 1; |\gamma|^2|\hat{\gamma}|^2) \tag{2}$$

The mean value given by [8]:

$$E\{|\hat{\gamma}|\} = \frac{\Gamma(N)\Gamma(3/2)}{\Gamma(N+1/2)} \times_3 F_2(3/2, N, N; N+1/2, 1; |\gamma|^2) \times (1-|\gamma|^2)^N \tag{3}$$

is different from the real value of the coherence $|\gamma|$. This means that the coherence estimator in Equation (1) is biased, and according to the results in Fig. 3, it can be seen that the bias decreases when the number of samples N increases. In the case of high real coherence values, the bias is lower as the two Pdf are well centered around the real value $|\gamma| = 0.8$. In the case of low coherence values, the coherence estimator displays a different behavior being significantly over-estimated. The mean value of the Pdf is far from the real coherence value $|\gamma| = 0.1$ and especially for $N = 9$. The coherence estimated with $N = 16$ more faithfully represents the coherence of the changed area ($|\gamma| = 0.1$), as there are fewer samples of high coherence value. According to Fig. 3, the use of a high number N leads to a better discrimination between changed ($|\gamma| = 0.1$) and unchanged ($|\gamma| = 0.8$) classes, but at the cost of losing spatial details [12].
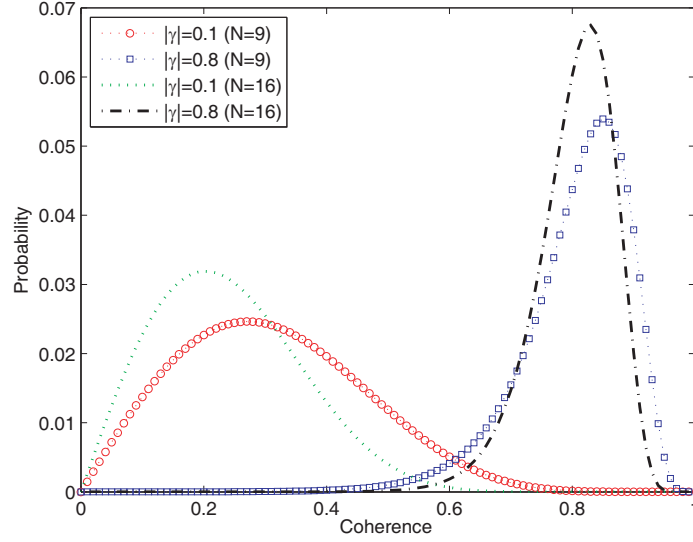
Figure 3. Probability density function of the estimated coherence $|\widehat{\gamma}|$ for different values of exact scene coherence $|\gamma|$ and N.

3.2. Methods for Reducing Coherence Bias

The results in Fig. 3 show the necessity of increasing the number of samples N to obtain a better separation between coherence values of the changed and unchanged areas.

A simple threshold applied to the coherence image may be used to distinguish between the changed and unchanged regions in the scene. To make a decision, the statistic z_1 is compared to a given detection threshold T_1:

$$z_1 = |\widehat{\gamma}| \underset{H_1}{\overset{H_0}{\gtrless}} T_1 \tag{4}$$

where H_0 is a realization of the null hypothesis (scene changes of interest is absent), and H_1 is the alternative hypothesis (scene changes of interest is present).

In change detection applications, the challenge consists in separating as much as possible the changed (i.e., low coherence) and unchanged pixels (i.e., high coherence) using a small window-size N to preserve detection of subtle changes as much as possible. It is important to note that when using real SAR images, the coherence bias causes the appearance of highly coherent pixels inside the changed area, thus considerably degrading the detection performance [10]. In what follows, we investigate two efficient methods of change detection performance improvement based on a coherence spatial averaging.

3.2.1. Averaged Magnitude Coherence

In order to improve the change detection performance, one can evaluate the mean of sample coherence over a K-pixel local area. This method, developed by Touzi et al. [8], was proposed as a bias removal of coherence estimate:

$$z_2 = \frac{1}{K} \sum_{i=1}^{K} |\widehat{\gamma}_i| \underset{H_1}{\overset{H_0}{\gtrless}} T_2 \tag{5}$$

3.2.2. Averaged Complex Coherence

The second method that was proposed by Touzi et al. [8] consists in averaging the complex values of the coherence as follows:

$$z_3 = \frac{1}{K} | \sum_{i=1}^{K} \widehat{\gamma}_i | \underset{H_1}{\overset{H_0}{\gtrless}} T_3 \tag{6}$$

Since the coherence phase ϕ is randomly distributed in the changed areas, the change statistic z_3 is more useful than z_2 as it uses a vector sum of coherence samples.

3.3. Change Detection Performance

In order to evaluate the change map quality independently from the detection threshold T, the evolution of the detection probability P_d as a function of the false alarm probability P_{fa} may be evaluated in the case where a set of constant thresholds are applied to the whole change map. These are the so-called Receiver Operating Characteristics (ROC) which correspond to the plots $P_d = f(P_{fa})$.

For a given threshold T, detection probability P_d and the corresponding false alarm P_{fa} are given by [16]:

$$P_d = \int_0^T P(\hat{\gamma}|\gamma = \gamma_{changed})d\hat{\gamma} \tag{7}$$

$$P_{fa} = \int_0^T P(\hat{\gamma}|\gamma = \gamma_{unchanged})d\hat{\gamma} \tag{8}$$

4. EXPERIMENTAL SETUP

The radar system used in our experiments was deployed indoors in the Microwaves and Radar Laboratory in the Military Polytechnic School of Algeria. The system uses low power pulsed transmitter connected to an antenna horn that is mounted on a rail of 0.9 m to scan in the azimuthal direction imaged gravel scene of 3.6 m width. A trihedral corner reflector was placed in the scene. The slant range to the scene center is approximately 4 m with a look angle of 30°. The parameters of the radar system are listed in Table 1. The acquisition system uses dual-channel sampler proving complex valued radar images of 340 pixels in the range direction and 600 pixels in the azimuth direction. As shown in Fig. 4(a), the radar intensity image of the corner reflector exhibits different behaviors along the two axes. In the range direction, the target is well located at approximately 1.5 m. This is due to the use of a pulse duration of 1 ns, which offers a range resolution $\delta_r = 15$ cm. In the azimuthal direction, the target is viewed by the radar during all the scan duration thanks to the real aperture of the radar antenna. It appears that the point spread function is irregular and vary from one position to another. This variation is well illustrated in the phase information in Fig. 4(b). Indeed, the Doppler shift of the radar echoes is maximum at the azimuthal positions $x = \pm 45$ cm and decreases to zero at $x \approx -7$ cm, where the radar velocity contains only a tangential component. In this work, the raw data have been processed using the RDA, CSA and ω-KA algorithms. According to Fig. 4(c), the reference target is well focused at its real azimuth position ($x \approx -7$ cm). When the results of the algorithms are compared based on the mainlobe -3 dB resolution, it appears that RDA, CSA and ω-KA offer the same performance. The results show that a synthetic aperture length of 90 cm permits an azimuth resolution $\delta_a \approx 4$ cm. It is important to

Table 1. Radar system parameters.

| Parameters	Value
Radar Frequency	9.6 GHz
Pulse width	1 ns
PRF	216 Hz
Range resolution	15 cm
Platform velocity	9 cm/s
Maximum aperture length	0.9 m
Swath	3.6 m
Look angle	30°
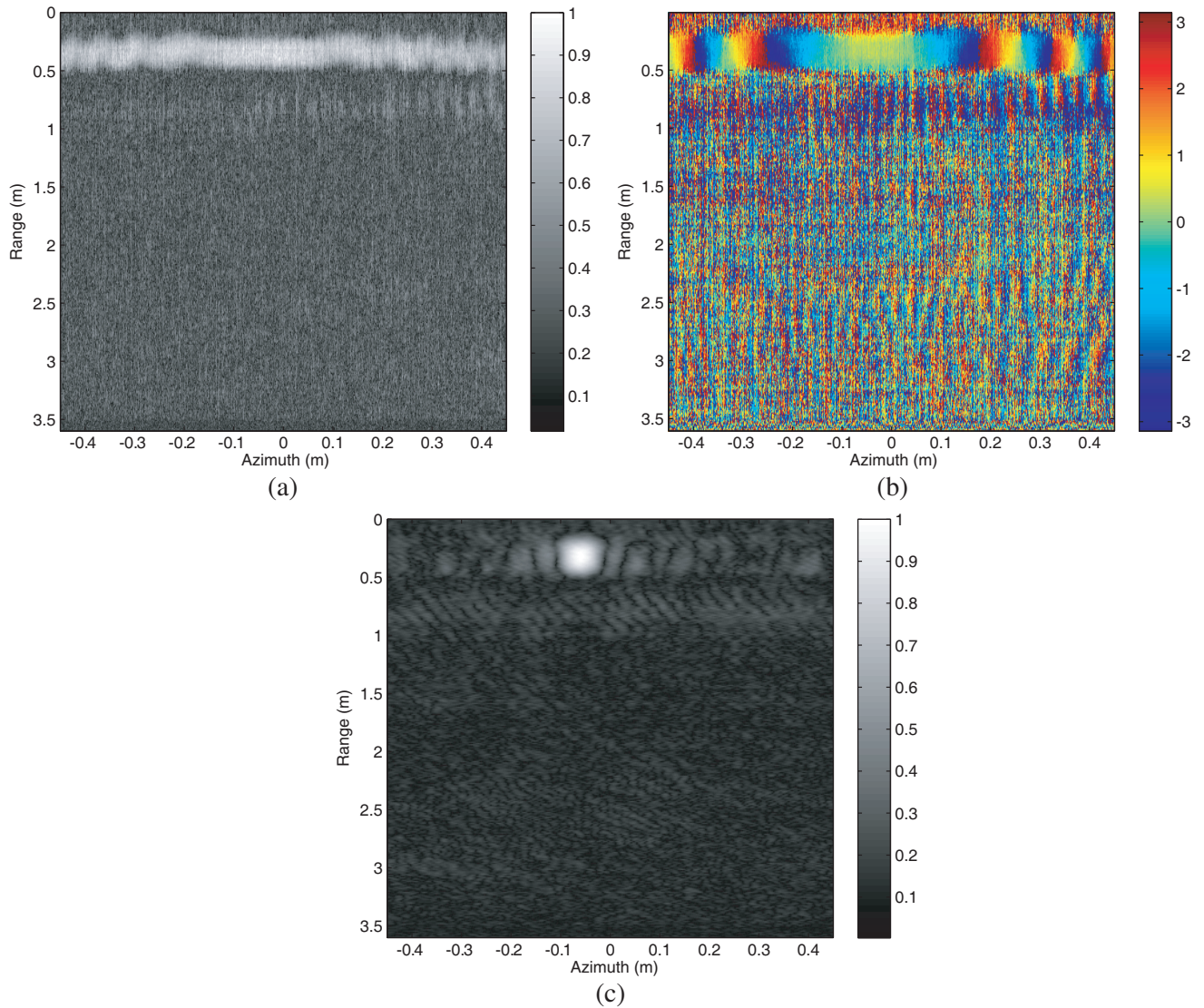
Figure 4. Complex radar image of the imaged target. (a) Normalized intensity image. (b) Phase (angle) image. (c) Focused SAR image.

note that the obtained SAR images are of very high resolution, since the image pixel is characterized by a spatial resolution (δ_r and δ_a) which is less than 20 cm. The results are also analyzed in terms of SAR image sensitivity, which is measured via Peak to Side Lobes Ratio (PSLR) and Integrated Side Lobes Ratio (ISLR) [15]. The values of PLSR and ISLR obtained using the three algorithms are acceptable (less than -20 dB) while the ω-KA algorithm offers the best performance.

The use of temporal multilooking improves the SAR image sensitivity as shown in Fig. 5(a), where the PSLR increase with the multilooking parameter M. The range patterns in Fig. 5(b) also show that the ground clutter is well estimated in the MLC SAR images. The results show that the parameter M does not affect the mainlobe -3 dB resolution.

The obtained radar data are also analyzed from the statistical point of view. As the SAR image pixels contain both amplitude and phase information, they are both analyzed and compared to theoretical results [16]. As shown in Fig. 6, the SAR amplitude is characterized by a Rayleigh distribution, while the SAR intensity (i.e., speckle) is exponentially distributed. The SAR phase is uniformly distributed without caring any useful information.
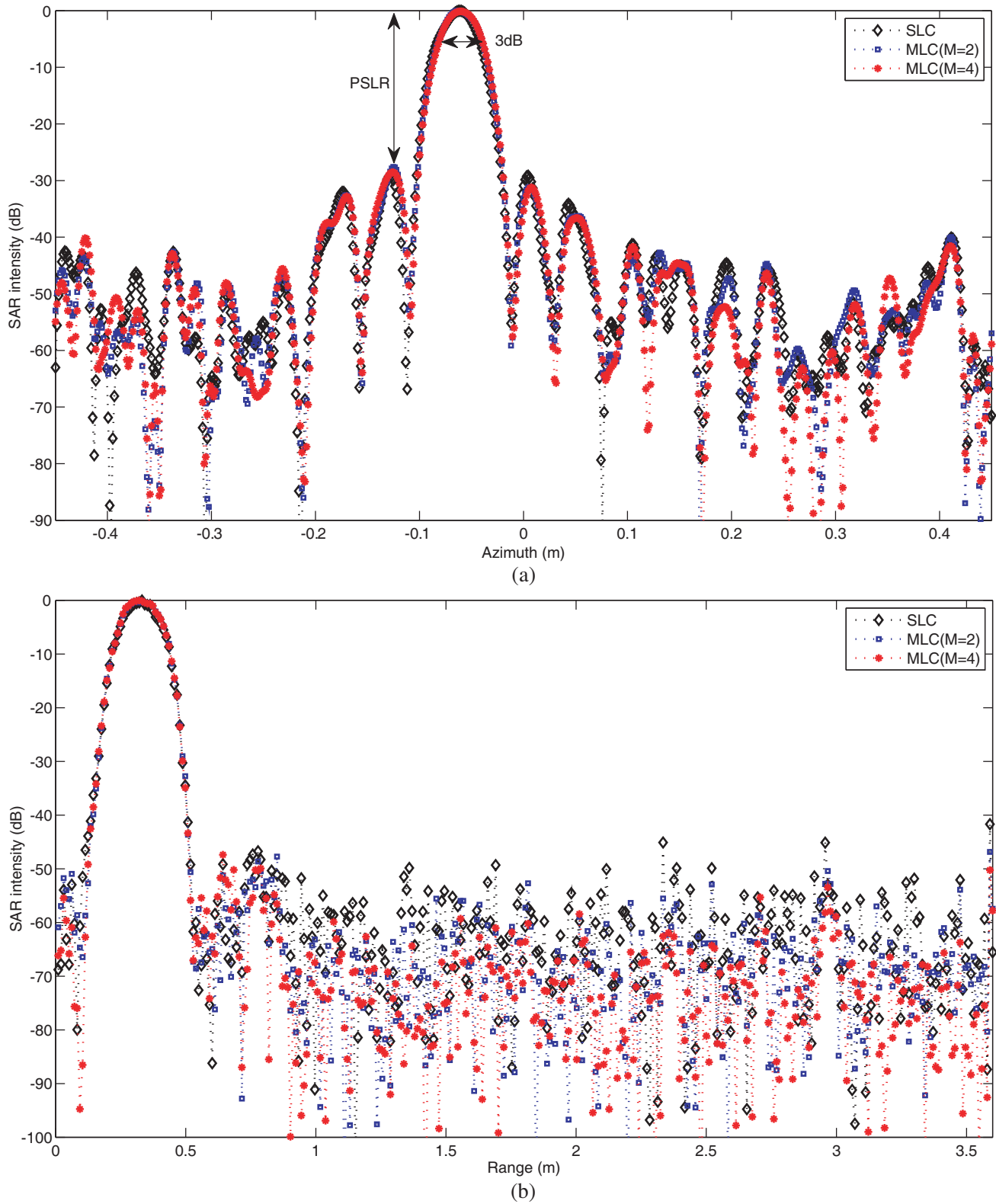
Figure 5. SAR intensity patterns across the reference target obtained using ω-KA. (a) Azimuth pattern. (b) Range pattern.
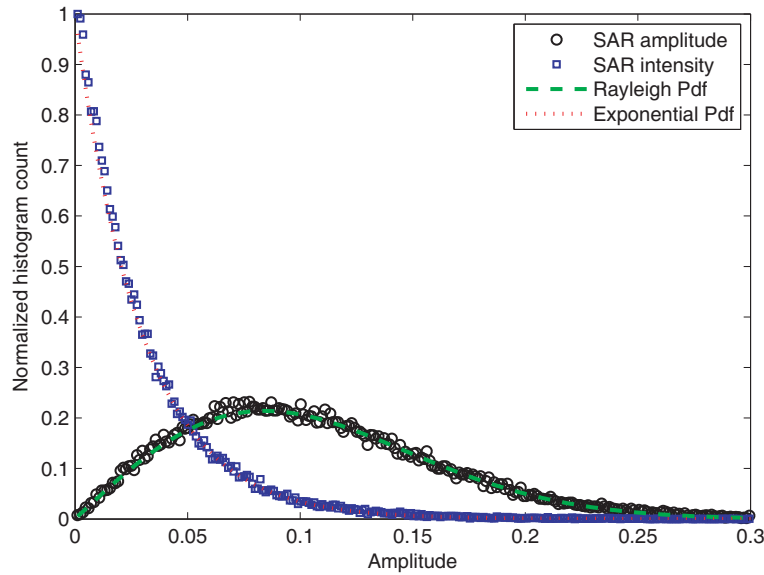
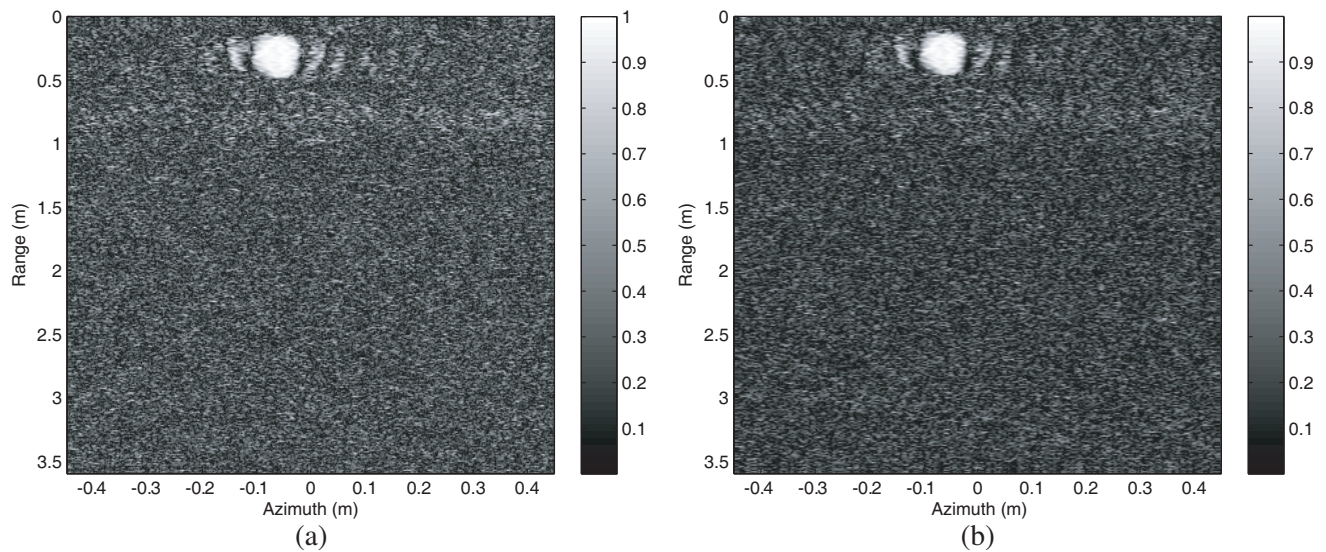**Figure 6.** SAR amplitude and intensity histograms.

Figure 7. Coherence magnitude using $N = 3 \times 3$. (a) SLC SAR images. (b) MLC ($M = 3$ looks) SAR images.

5. CCD PERFORMANCE ANALYSIS

The SAR coherence presents the advantage of being able to detect subtle ground changes that are not visible in the two SAR intensity images (a kind of change that is only revealed by the InSAR phase) [12].

In the present work, coherence images need to be estimated for various values of parameters M, N and K. For that purpose and after the acquisition of the first radar image, the gravel scene was voluntarily disturbed without affecting the ground target. Fig. 7(a) shows the coherence map corresponding to the SAR image in Fig. 4(c). One can notice that the reference target is characterized by high coherence values (bright pixels) while the rest of the imaged gravel scene is clearly indicated by low coherence values (dark pixels). However, highly coherent pixels (white colored pixels) appear inside this changed area, a fact due to the limited window-size (of N samples) in the numerical computation of
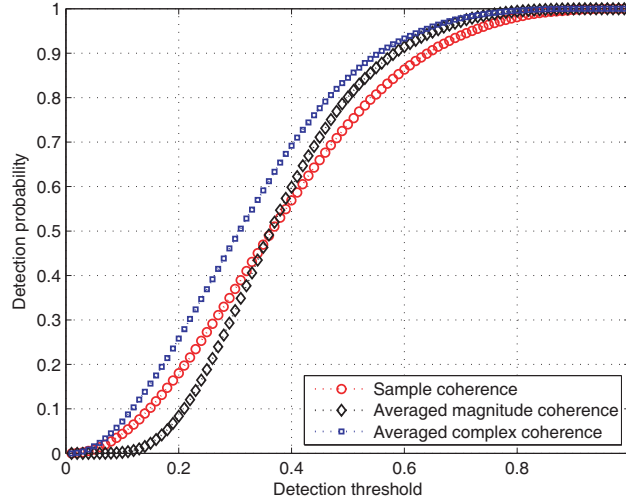
Figure 8. Detection probability versus detection threshold for the detection statistics $z_{i,\ i=1:3}$. $N = 9$ and $M = 1$.
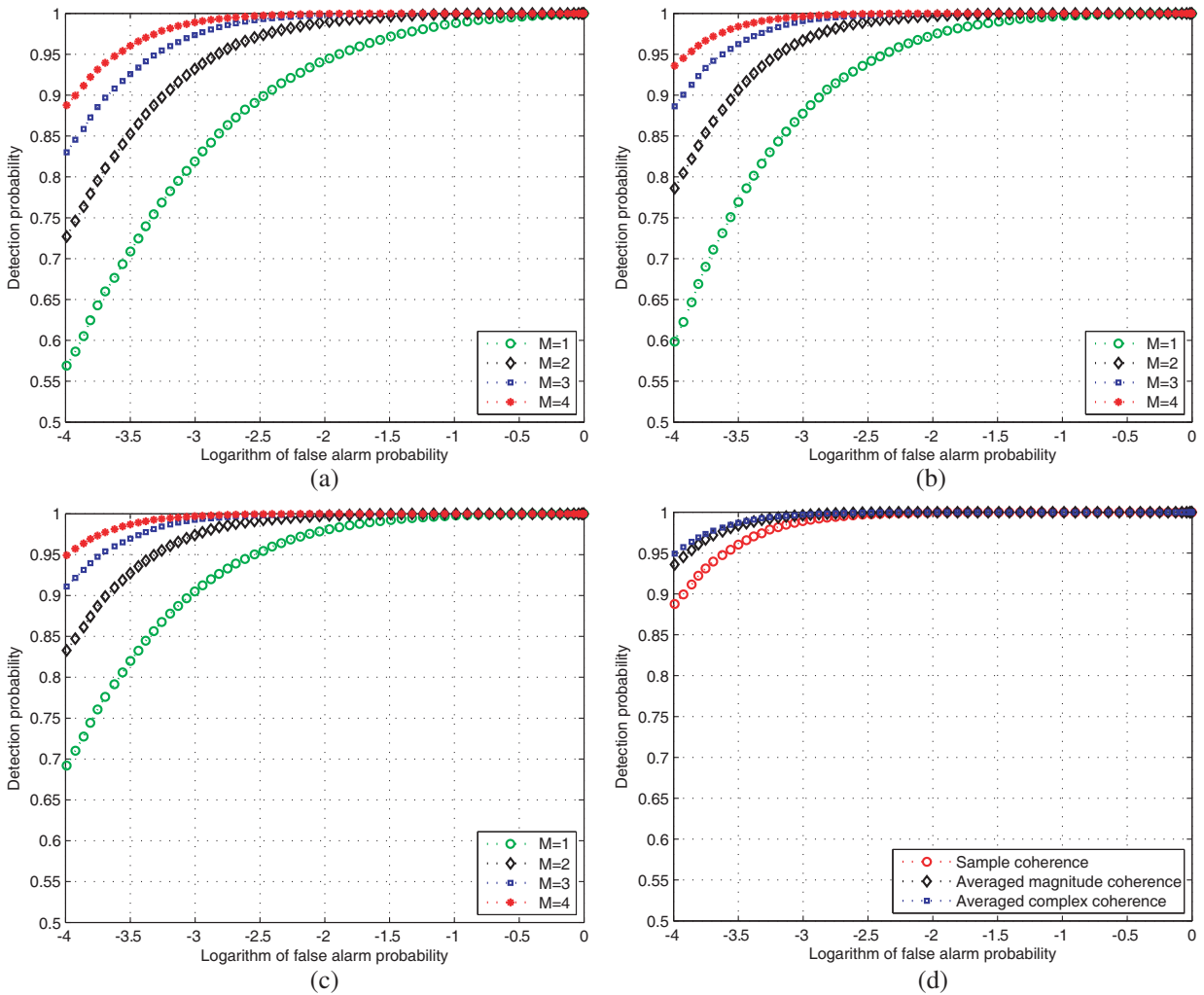
Figure 9. ROC curves corresponding to different detection statistics. (a) z_1 with $N = 9$. (b) z_2 with $N = 9$ and $K = 9$. (c) z_3 with $N = 9$ and $K = 9$. (d) z_1, z_2 and z_3 with $M = 4$ looks.

Equation 1. Fig. 7(b) shows coherence image corresponding to the use of SAR MLC images. It can be seen that the coherence estimation of the changed area is improved and the number of highly coherent pixel are drastically reduced.

In order to distinguish between the changed and unchanged regions in the scene, a fixed threshold must be applied to the statistics $z_{i,\ i=1:3}$. As the values of the statistics $z_{i,\ i=1:3}$ are between 0 and 1, the detection threshold values $T_{i,\ i=1:3}$ are also in the same range. For each possible value of T_i, one can evaluate the detection probability P_d that corresponds to the number of detected changed pixels inside the disturbed area [10]. As shown in Fig. 8, for each statistic z_i, the detection probability P_d improves with an increase of the threshold value T_i. Unfortunately, this also increases the false alarm probability P_{fa}, which corresponds to the number of detected changed pixels inside the undisturbed area. A good detection technique is one offering simultaneously the highest P_d and the lowest P_{fa}. So to quantify the detection performance, we must simultaneously assess P_d and the corresponding P_{fa} for each statistic.

The obtained ROC curves corresponding to the use of the statistic z_1 are depicted in Fig. 9(a). The procedure that is used to evaluate experimentally the ROC curves is well described in [10]. Typically the useful variation range for P_{fa} is $[10^{-4},\ 10^{-3}]$. This corresponds to the situation where from 1 to 10 pixels may be declared as changed in an area of 100×100 unchanged pixels.

Figure 9(b) shows the detection performance improvement when using MLC SAR images. Indeed, in the case of low P_{fa}, one may achieve a P_d improvement of nearly 30% for $M = 2$ and 60% for $M = 4$. The detection performance improves when using the two statistics z_2 and z_3. As depicted in Figs. 9(b) and (c), the averaged based coherence statistics provide important detection performance improvement and especially for $M = 2$ and $M = 3$ looks. For high value of the temporal multilooking (e.g., $M = 4$ looks), the two statistics z_2 and z_3 tend to provide the same detection performance as in 9(d). In this situation and for $P_{fa} = 10^{-3}$, the changes are almost detected with $P_d \approx 1$.

6. CONCLUSION

In the present work, we investigate detection performance improvement throughout the use of SAR MLC images. After the SAR image formation using three focusing algorithms, the problem of coherence misestimation is described and illustrated. Various statistics that reduce the coherence bias and improve the change detection performance are analyzed. The results show that the use of MLC SAR images with only four looks is sufficient to detect the entire fine changes ($P_d \approx 1$) in the case of a low false alarm rate. Further research using spaceborne or airborne radar systems could show the usefulness of the MLC SAR data for producing reliable and robust change detection maps.

REFERENCES

1. Curlander, J. C. and R. N. McDonough, *Synthetic Aperture Radar, Systems and Signal Processing*, John Wiley & Sons, NY, 1991.
2. Massonnet, D. and J. C. Souyris, *Imaging with Synthetic Aperture Radar*, EPFL Press, 2008.
3. Zebker, H. A. and R. M. Goldstein, "Topographic mapping from interferometric synthetic aperture radar observations," *J. Geophysics Research*, Vol. 9, No. 5, 4993–4999, 1986.
4. Massonnet, D. and K. L. Feigl, "Radar interferometry and its applications to changes in the Earth's surface," *Review of Geophysics*, Vol. 36, 441–500, 1998.
5. Preiss, M., D. A. Gray, and N. J. S. Stacy, "Detecting scene changes using synthetic aperture radar interferometry," *IEEE Transactions on Geoscience and Remote Sensing*, Vol. 44, No. 8, 2041–2054, 2005.
6. Fan, C., X.-T. Huang, T. Jin, J.-G. Yang, and D. X. An, "Novel pre-processing techniques for coherence improving in along-track dual-channel low frequency SAR," *Progress In Electromagnetics Research*, Vol. 128, 171–193, 2012.
7. Jungkyo, J., et al., "Damage-mapping algorithm based on coherence model using multitemporal polarimetric interferometric SAR data," *IEEE Transactions on Geoscience and Remote Sensing*, 2017, DOI: 10.1109/TGRS.2017.2764748.

8. Touzi, R., A. Lopes, J. Bruniquel, and P. W. Vachon, "Coherence estimation for SAR imagery," *IEEE Transactions on Geoscience and Remote Sensing*, Vol. 37, No. 1, 135–149, 1999.

9. Martinez, C. L., "Coherence estimation in synthetic aperture radar data based on speckle noise modeling," *Applied Optics*, Vol. 46, No. 4, 544–558, 2007.

10. Bouaraba, A., D. Borghys, A. Belhadj-Aissa, M. Acheroy, and D. Closson, "Improving CCD performance by the use of local fringe frequencies," *Progress In Electromagnetics Research C*, Vol. 32, 123–137, 2012.

11. Bouaraba, A., et al., "InSAR phase filtering via joint subspace projection method: Application in change detection," *IEEE Geoscience and Remote Sensing Letters*, Vol. 11, No. 10, 1817–1820, 2014.

12. Bouaraba, A., et al., "man-made change detection using high resolution Cosmo-SkyMed SAR interferometry," *Arabian Journal for Science and Engineering*, Vol. 41, No. 1, 201–208, 2016.

13. Wahl, D. E., D. A. Yocky, C. V. Jakowatz, and K. M. Simonson, "A new maximum-likelihood change estimator for two-pass SAR coherent change detection," *IEEE Transactions on Geoscience and Remote Sensing*, Vol. 54, No. 4, 2460–2469, 2016.

14. Karsten, S. and H. Andrew, "InSAR processing for volcano monitoring and other near-real time applications," *Journal of Geophysical Research: Solid Earth*, Vol. 121, No. 4, 2947–2960, 2016.

15. Cumming, I. G., et al., "Interpretations of the Omega-K algorithm and comparisons with other algorithms," *IEEE Geoscience and Remote Sensing Symposium Proceedings*, 1455–1458, 2003.

16. Richards, M. A., *Fundamentals of Radar Signal Processing*, McGraw-Hill, New York, 2005.